ULTRAFINE DUCTILE AND AUSTEMPERED DUCTILE IRONS BY SOLIDIFICATION IN ULTRASONIC FIELD

M. Ahmed
Institute of Manufacturing Technology and Quality Management, Otto-von-Guericke-University, Universitätsplatz 2, 39106 Magdeburg, Germany
Department of Foundry Technology, Central Metallurgical Research and Development Institute, Helwan, Cairo 11421, Egypt

E. Riedel and R. Bähr
Institute of Manufacturing Technology and Quality Management, Otto-von-Guericke-University, Universitätsplatz 2, 39106 Magdeburg, Germany

M. Kovalko and A. Volochko
The Physical-Technical Institute, National Academy of Science, Kuprevich str. 10, 220141 Minsk, Belarus

A. Nofal
Department of Foundry Technology, Central Metallurgical Research and Development Institute, Helwan, Cairo 11421, Egypt

https://doi.org/10.1007/s40962-021-00683-8

Abstract

In this research, ultrasonic melt treatment (UST) was used to produce a new ultrafine grade of spheroidal graphite cast iron (SG iron) and austempered ductile iron (ADI) alloys. Ultrasonic treatment was numerically simulated and evaluated based on acoustic wave streaming. The simulation results revealed that the streaming of the acoustic waves propagated as a stream jet in the molten SG iron along the centerline of the ultrasonic source (sonotrode) with a maximum speed of 0.7 m/s and gradually decreased to zero at the bottom of the mold. The metallographic analysis of the newly developed SG iron alloy showed an extremely ultrafine graphite structure. The graphite nodules' diameter ranging between 6 and 9 µm with total nodule count ranging between 900 to more than 2000 nodules per mm^2, this nodule count has never been mentioned in the literature for castings of the same diameter, i.e., 40 mm. In addition, fully ferritic matrix was observed in all UST SG irons. Further austempering heat treatments were performed to produce different austempered ductile iron (ADI) grades with different ausferrite morphologies. The dilatometry studies for the developed ADI alloys showed that the time required for the completion of the ausferrite formation in UST alloys was four times shorter than that required for statically solidified SG irons. SEM micrographs for the ADI alloys showed an extremely fine and short ausferrite structure together with small austenite blocks in the matrix. A dual-phase intercritically austempered ductile iron (IADI) alloy was also produced by applying partial austenitization heat treatment in the intercritical temperature range, where austenite + ferrite + graphite phases coexist. In dual-phase IADI alloy, it was established that introducing free ferrite in the matrix would provide additional refinement for the ausferrite.

Keywords: *ultrasonic melt treatment UST, spheroidal graphite iron, austempered ductile iron, dual-phase ADI alloys, CFD simulation, extremely fine graphite, ultrafine ausferrite structure, nodularity and nodule count*

Received: 11 June 2021 / Accepted: 23 August 2021 /
Published online: 11 October 2021

Introduction

Spheroidal graphite irons (SG iron), also known as ductile irons (DI), and austempered ductile iron (ADI) alloys are widely used in different industrial sectors. SG iron alloys have an adequate variety of mechanical and physical properties such as fracture toughness, design flexibility, castability, cost-effectiveness arising from low melting and pouring temperatures, and excellent machinability properties.[1] ADI alloys are produced by an isothermal austempering heat treatment. The austempering process of ductile iron alloys results in developing a series of materials with a unique combination of mechanical and physical properties. Therefore, ADI alloys became a strong competitor for steel castings and forgings. The conventional austempering heat treatment of ADI consists of two consecutive steps: austenitization and austempering. The heat treatment starts with austenitizing the castings at high temperature ranging between 850 and 950 °C then quenching in a salt bath at temperatures ranging between 250 and 400 °C. The final microstructure is spheroidal graphite in ausferritic matrix (ferrite needles + high carbon stabilized austenite).[2,3]

One important factor that defines the mechanical properties of both SG irons and ADI alloys is the graphite morphology.[4–7] According to ASTM standard E2567-16a,[8] the graphite morphology is characterized by two special variables: nodule count and nodularity. These two variables are responsible for delineating the final microstructure and controlling the quality of the produced SG irons.[5,9–12] Gue et al.[4] demonstrated that the graphite morphology as well as microstructure constituents influence the mechanical properties such as hardness, strength and elongation of the SG irons. Pedersen et al.[13] and Sosa et al.[14] established that high nodule count in the matrix is required at high cooling rate conditions to prevent carbides formation in the final microstructure. Moreover, high nodule count also improves the fatigue and compression strength of the SG irons.[15,16] For ADI alloys, high nodule count of the spheroidal graphite could accelerate the transformation kinetics by increasing the rate of carbon diffusion.[17,18] Fraś et al.[18] reported that ADI with extremely high nodule counts, as in the case of thin walled ADI parts, the time required for austenitization and austempering is significantly reduced when compared with conventional ADI alloy. The short distance between the graphite spheroids reduces the carbon diffusion path, which effectively enhances the austemperability. Therefore, it is presumable to exclude the alloying additions with expensive elements such as Ni, Cu and Mo used for improving the austemperability. It should be mentioned that austemperability enhancement is resulted from the segregation reduction, which means more uniform distribution of elements concentration. In addition, it was reported that[19,20] increasing the nodule count extremely refines the ausferrite structure in the matrix. Consequently, this leads to improve both strength and ductility of the produced ADI parts.

Nowadays, the metal casting industry is finding increasing applications for ultrasonic treatment due to both economic as well as technological aspects such as energy efficiency and environmental friendliness together with the ability to reach the finest possible grain size without using special harmful additions. This would explain why many researchers devoted their efforts to study the effect of UST on different light alloys, especially aluminum alloys.[21–26] However, this is not the case with the iron and steel alloys, just very few researches were conducted to apply the UST in molten iron and steel.[27–31]

The main idea of using UST is to apply some dynamic action into the molten metal to improve the final properties of the materials. The main basics of ultrasonic treatment are acoustic streaming and cavitation. Cavitation means the formation and impulsion of microbubbles in the molten metal.[32,33] Over a specific value of the amplitude of acoustic pressure, acoustic stream jet initiates and starts to propagate inside the melt causing a circulation movement in the molten metal. Due to the interaction between the acoustic waves and the viscous force of the melt, the ultrasonic stream jet is attenuated causing a variation in the acoustic pressure along with the propagation direction. Furthermore, the acoustic stream jet accelerates the melt flow making the temperature of the molten metal and distribution of the solutes much more homogeneous. Homogeneous temperature inside the molten metal promotes more even grain growth along various directions.[22]

In iron and steel melts, the cavitation bubbles are considered to be bubbles of oxygen dissolved in the molten metal.[27,28] These oxygen bubbles are formed and grew up by inertia under the compression stress during the compression half-period of the sinusoidal oscillation. After many compression and tensile stress cycles, the oxygen bubbles impulse and produce an intensive shockwave in the melt. The produced shock waves are responsible for crystal fragmentation which leads to multiplying the nucleation sites.[22,24,33] This may explain the resulted fine microstructure found in different UST samples. Yoshiaki et al.[27] studied the effect of ultrasonic processing on gray iron and SG cast iron. The results related to the SG iron samples revealed that the UST provided a fine graphite structure. The diameter of the fine spheroidal graphite was about 13 μm, and the total number of the spheroids was about three times higher than conventional castings. Voigt et al.[31] studied the effect of the non-contact ultrasonic treatments during the solidification of gray and SG irons. The non-contact acoustic inoculation of the gray irons was found to act either as supplement to or a replacement of conventional chemical inoculation, where undercooled type D-graphite and chill formation could be remarkably decreased or eliminated. Furthermore, only slight changes in the graphite morphology were observed in the UST SG irons. Recently, it was found that thermomechanical treatment[34,35] or performing very long austempering time[36]

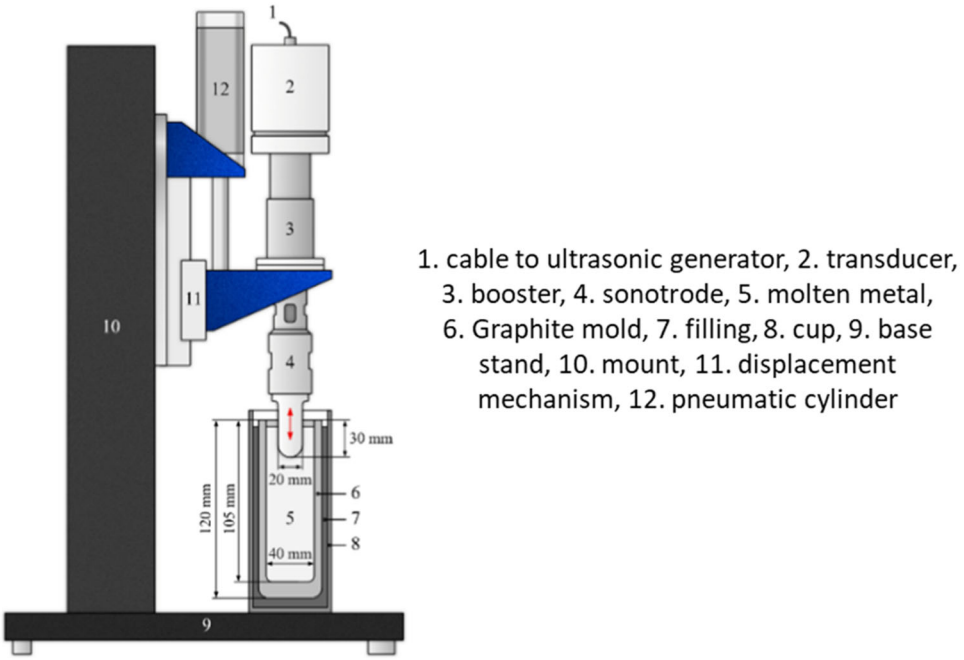

Figure 1. The experimental setup for the ultrasonic treatment of SG iron.

could lead to evolution of a novel nano-scale ADI microstructure, with an exceptional combination of strength and ductility properties.

Accordingly, the purpose of this investigation was to produce SG irons and ADI alloys with an extremely ultrafine graphite and ausferrite structure by using ultrasonic treatment technology (UST) during solidification of the molten metal. This approach seems easier to implement than the thermomechanical treatment and more economic than performing very long austempering time. Moreover, different austempering heat treatment cycles were performed to produce several grades of ADI alloys. The kinetics of transformation during austempering were also studied using a high accuracy quenching dilatometry. Optical microscope and scanning electron microscope were used to evaluate the effect of UST on the graphite morphology as well as analyze the microstructure development for the investigated alloys. Finally, the ultrasonic streaming phenomenon in the molten iron was numerically simulated using a new computational fluid dynamic modelling (CFD) recently developed by Riedel et al.[37,38] This new model helps to better understanding some of the acting mechanisms of dynamic solidification in molten metals as well as defines the optimum casting and UST parameters to achieve the finest possible structure.

Experimental Setup

Melting and UST Treatment

A schematic drawing of the experimental setup is shown in Figure 1. The melting and casting process of this investigation were made using a medium frequency 5-Kg induction furnace. The main raw materials used to give the final chemical composition were 40% steel scrap and 60% high purity pig iron-HPPI. The chemical composition of the charge materials as well as the final chemical composition of the produced castings are indicated in Table 1. The additions charged into the furnace were synthetic graphite carburizer (99% carbon) and Fe-Si (65% Si). After complete melting and deslagging processes, spheroidization and inoculation were performed when the molten metal temperature reached (1520 °C). The sandwich process had been used for spheroidization and inoculation treatments, where the molten metal was treated with magnesium as Fe-Si-Mg (9% Mg) alloy required for graphite spheroidization.

Table 1. Chemical Composition of the Raw Materials and the Investigated Iron

Sample	C	Si	Mn	P	S	Cr	Cu	Mg	Ti	Fe
Steel scrap	0.13	0.058	0.53	<0.007	<0.03	0.015	0.012	–	0.002	Bal.
High purity pig iron	3.80	0.15	0.02	<0.03	<0.025	0.014	0.003	0.036	0.04	Bal.
S.G iron	3.65	2.52	0.29	0.0236	0.0158	0.024	0.01	0.048	0.032	Bal.

In this process, Fe-Si-Mg was introduced in a pocket built into the ladle bottom and covered with high quality low carbon steel turnings, which acted as a physical barrier between the Fe-Si-Mg alloy and incoming molten iron to delay the reaction time and increase efficiency in terms of alloy use (magnesium recovery), as well as giving a reduction in flame and flaring. Two identical graphite molds were preheated and prepared for the pouring: one mold represented the static solidification condition and designated as (SG-S.S), while the other mold positioned under an ultrasonic system and marked as (SG-U.S). Finally, the molten iron was poured at temperature 1400 °C into a preheated graphite mold (400 °C).

The ultrasonic system with potential power of 1 KW with a 20 kHz frequency had been used for the molten iron treatment. A titanium sonotrode with 20 mm diameter was used. The sonotrode was preheated at 400 °C using a vertical tubular furnace to avoid the thermal shocking when contacting with the molten metal and to obviate an extremely fast cooling at the tip area. During UST, the sonotrode was positioned in the center of the graphite mold and deepened 30 mm from the top of the mold. The recorded ultrasonic power was approx. 700 W, and the measured peak to peak amplitude was 20 μm.

The relatively high Ti-content of the produced SG iron compared to that of the steel scrap is the result of using high amounts of high purity pig iron, containing ~ 0.04 w.t % Ti. Such grades of pig iron are usually obtained as a by-product during extraction of titanium from Fe-containing titanium ores.

Dilatometry Studies

Dilatometry is considered as one of the most important techniques for phase transformation investigations in Fe-C alloys. In this work, the dilatometry experiments were conducted to produce different austempered ductile iron (ADI) samples and to study the influence of the graphite morphology on the ausferrite transformation, in terms of transformation rate and time. Dilatometry tests were performed using Quenching LINSEIS L87/RITA dilatometer. Cylindrical specimens with 3 mm diameter and 10 mm length were heated in a vacuum chamber by induction (2.2 MHz) with heating rate 0.2 K/sec to 900 °C and held for 10 minutes at this temperature. After that, high quenching rate was applied using helium gas at 50 K/sec to the targeted austempering temperature (275 °C and 375 °C) and the samples were held at these temperatures for around 60 minutes. In addition, other SG iron samples were partially austenitized within the intercritical eutectoid region at 820 °C, where austenite (γ) + ferrite (α) + graphite (G) coexist. Further quenching at 325 °C could introduce proeutectoid ferrite in the ADI matrix which is responsible for improving the toughness and machinability properties of the ADI.[39–41] This grade of ADI is referred as intercritically austempered iron (IADI) or dual-phase (DP) ADI. Finally, the samples were air cooled to the room temperature, and the change in length was recorded with temperature and time using a computer-controlled test cycle.

Metallographic Investigation

The metallographic analysis was conducted to examine the microstructure constituents for the ADI alloys as well as to evaluate the graphite morphology of the SG irons in terms of nodule count and nodularity. All investigated samples were prepared using the conventional preparation steps which consisted of mounting, grinding, polishing, and etching by using a 3% nital solution. The microstructural characteristics were evaluated using a digital microscope, KEYENCE VHX-5000. Nodule count and nodularity were calculated using an image analyzer software, ZEISS according to ISO 945-1 and ISO 945-4. Grenier et al.[42] extensively described and analyzed the nodule count measurement method using image analysis. In this investigation, nodule count was measured at magnification of 100x and a trap size of 15 μm^2 was selected. Deep etched samples were also prepared for the scanning electron microscopy (SEM) using FEI XL30 ESEM equipped with an EDS analyzer. EBSD investigation also conducted using FEI Scios DualBeam (Thermo Fisher Scientific, Waltham, MA, USA) equipped with an EBSD (AMETEK-EDAX, Hikari Kamera, TSL-OIM 7) to evaluate the structure characteristics of the ausferrite as well as phase distribution.

Microhardness Testing

Vickers microhardness testing was performed to measure the microhardness values of the produced ADI samples. The microhardness test was carried out at room temperature with a load of 1.961 N (HV 0.2) and load time of 15 sec by using a microhardness tester SHIMADZU HMV (SHIMADZU, Kyoto, Japan).

CFD- Simulation Model Description

A simple CFD model was created to analyze the ultrasonic streaming velocities inside the molten iron. This model was solved and analyzed using a commercial CFD simulation software called FLOW-3D® v12.0[43] and FlowSight® v12.0.[44] The geometry dimensions used for the simulation setup are shown in Figure 2. The ultrasonic titanium radiator with 20 mm diameter was immersed in 30 mm depth inside the molten metal and positioned in the middle of a graphite mold. The internal volume of the graphite mold is 60×60×105 mm with 10 mm wall thickness. The

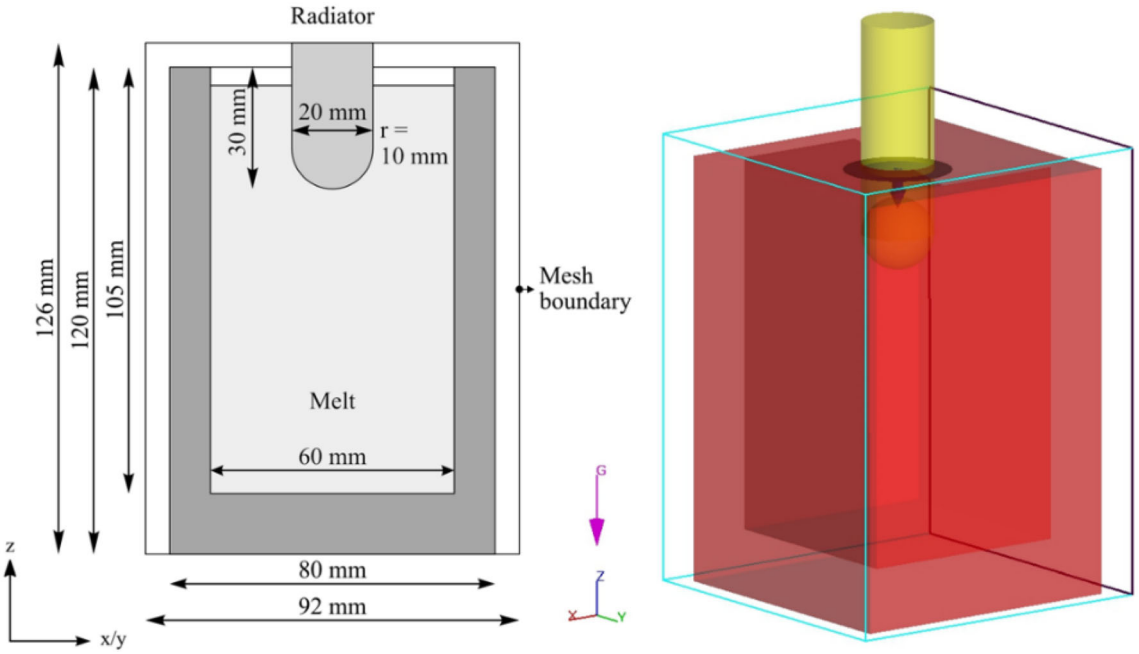

Figure 2. Schematic drawing of the geometry model.

Table 2. Fluid Parameters Required for CFD Calculations

Parameter	SG irons-GJS-400
-Density $_{Liquid}$, kg/m^3	6768
-Density $_{Solid}$, kg/m^3	7150
-Viscosity, kg/m/s	0.0047
-Surface tension coefficient, kg/s^2	0.80
-Contact angle, degree(s)	110
-Thermal conductivity, W/m/K	35,0
-Liquidus temperature, K	1437 (1164 °C)
-Solidus temperature, K	1416 (1143 °C)
-Latent heat of fusion, J/kg	2,5e+05

molten iron was treated as a limited compressible fluid, and the starting pouring temperature was 1673 K (1400 °C). The other fluid parameters used in the CFD calculation are listed in Table 2. The acoustic waves were introduced into the fluid through the sonotrode. Sinusoidal oscillation[45] of the radiator had been used for that purpose; a general moving object (GMO) was activated in the software. GMO model permits the position of any axis or any fixed point to be arbitrary. The expression for a sinusoidal angular velocity, (ω) component in z-direction is as follows:[43]

$$v(t) = \omega.s_0.\cos(\omega t + \phi_0) \quad \text{Eqn. 1}$$

$$\omega = 2\pi f \quad \text{Eqn. 2}$$

The values for amplitude, s_0; frequency, f; phase angle, and ϕ_0 are required as input data to the GMO model.

Results and Discussion

Simulation Analysis

The numerical simulation of the acoustic streaming velocity and its distribution in the molten iron are shown in Figure 3. The acoustic streaming propagates in the melt like a stream jet along the centerline of the sonotrode and gradually decreases to zero at the bottom of the mold. The maximum velocity $\approx$ 0.7 m/sec appears in the area near to the sonotrode and extends to about 30 mm below the sonotrode. The molten metal acceleration is controlled by the acoustic stream pressure, gravity, and the viscous force. The velocity of the stream jet attenuated gradually when the stream jet propagates downward. This happens because of the viscous force of the molten metal becomes higher than the sum of the acoustic stream pressure and the gravity force.[28,30,46] It is also noticed that with further progress of the solidification process, the ultrasonic treatment effect in the melt faded. This is a result of increasing the viscosity of the melt due to increasing the weight of the solid fraction. Figure 3c illustrates the streamline in the molten iron. It is obvious that when the stream jet reaches the bottom of the mold, it swept away at the edges forming a vortex flow, causing a circulation and mixing movement in the melt. The same streaming behavior is observed by Kang et al.[30] in a molten steel. It is hypothesized that as the viscosity force is much higher near the mold wall besides the effect of the gravity, the stream jet cannot reach the top surface, rather it flows upward and forms a radial symmetrical vortex near the bottom edges of the mold.

In statically cooled iron, the solids begin to develop from the bottom of the mold and then grow gradually until the

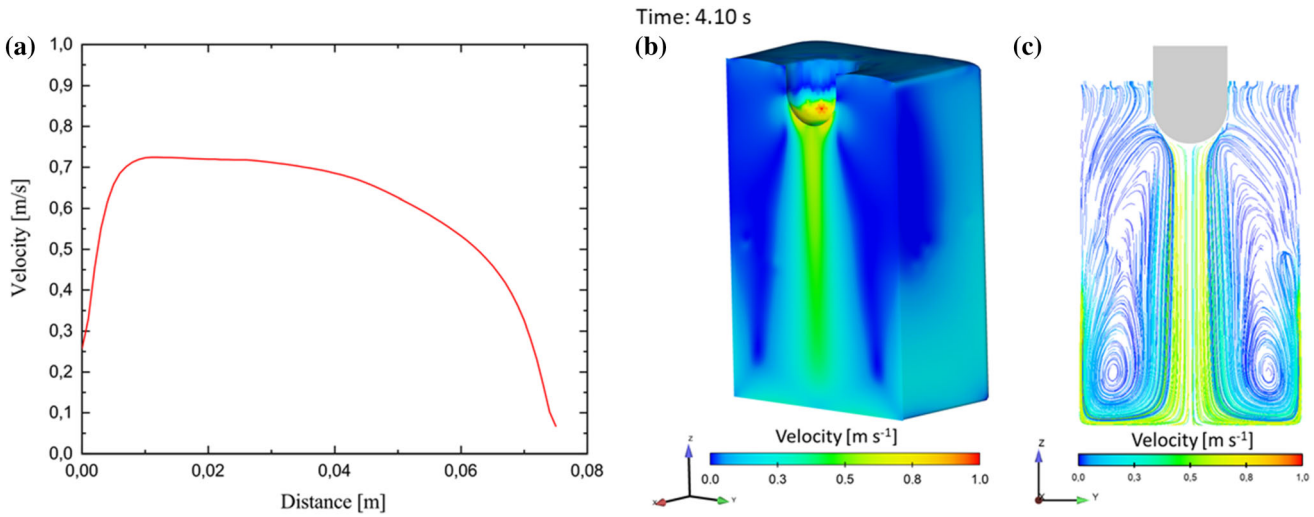

Figure 3. (a) Velocity distribution in the fluid along z-direction during UST, (b) cross section representing the propagation of the acoustic stream jet, and (c) streamline of the acoustic flow in the investigated molten SG iron.

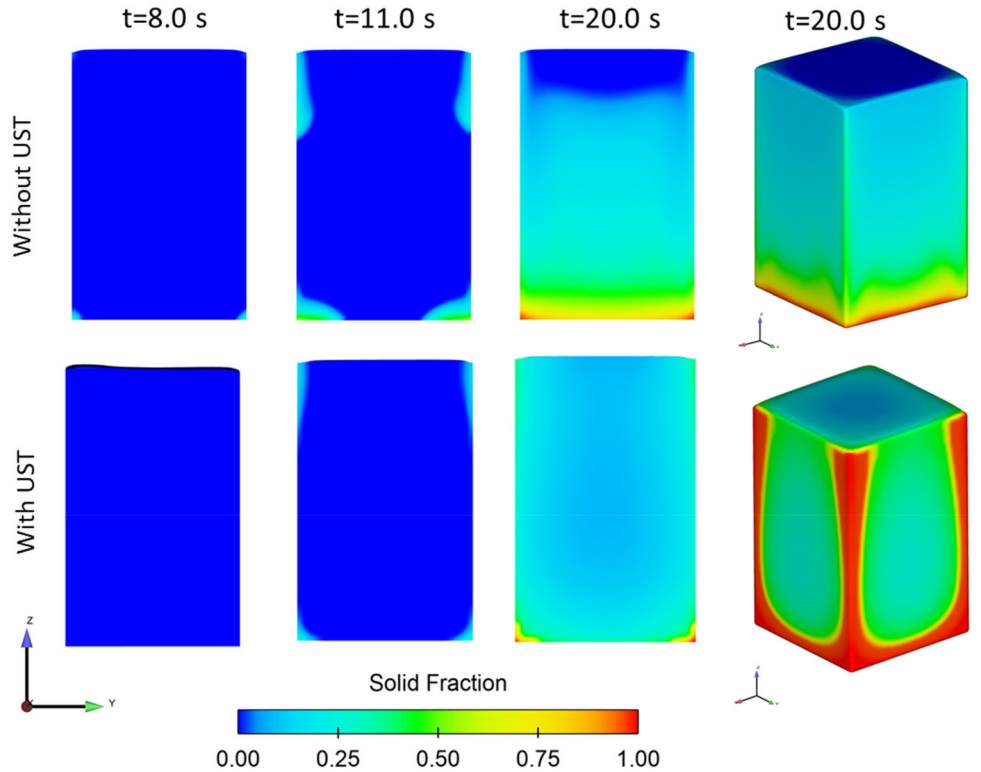

Figure 4. 2D/3D models illustrating the solid/liquid fraction distribution in the mold.

solidification ends at the top surface of the mold (see Figure 4). However, applying ultrasonic treatment slows down the solidification rate at the beginning of the solidification process when compared with the statically cooling process. After few seconds, ultrasonic stream waves significantly increase the heat transfer coefficient in the melt making the solidification rate going rapidly and solids grow more homogenously than that observed in the statically cooled iron. A good agreement is noticed between the simulation results depicted in Figure 3c and Figure 4. Due to the spread of the ultrasonic stream waves in the middle of the mold, the solidification process under UST begins from the bottom of the mold as well as from the mold's walls until the solidification ends at the center of the top surface of the mold. The fact that the solidification starts from the wall of the mold could explain the vortex flow formed during UST; in addition, it supports simulation flow model shown in Figure 3 and also the hypothesizes made by Kang et al.[30]

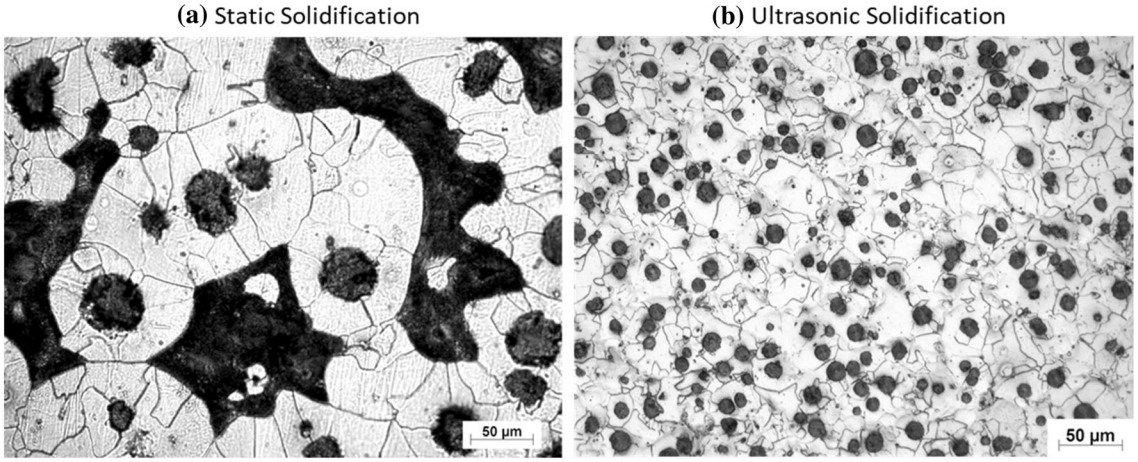

Figure 5. Microstructure obtained from the SG iron samples, (a) static condition and (b) UST condition.

Table 3. Microstructure Evolutions of the SG Iron Produced Under Static and UST Conditions

Sample	Ferrite, %	Pearlite, %	Graphite Area, %	Nodule Count, nodules per mm^2	Nodule Size, µm	Sphericity, %
SG iron - Static	67	23	10	270	17–55	~ 90
SG iron - UST	85	–	15	956–2175*	6–9	~ 93

*The measured nodule count of the UST irons is varied according to the measuring location (see Figures 6 and 7).

**The measured values are the average of five fields of view.

Graphite Morphology

Figure 5a shows the optical micrographs for the SG irons solidified under static condition. In statically solidified SG iron, the microstructure consists of around 10% well spheroidized graphite in a matrix of 67% ferrite, 23% pearlite as revealed by the image analysis software. In addition, the measured nodule count is 270 nodules per mm^2 with about 92% sphericity. The graphite size falls in two different groups, relatively coarse and fine nodules. The relatively coarse nodules are primary graphite nodules formed in the liquid iron of hypereutectic composition with carbon equivalent (C.E) = $C + \frac{Si}{3} \approx 4.5$ %.[1] The primary graphite nodules have more chance to grow, until the eutectic temperature is reached, where the eutectic mixture of graphite nodules enveloped with austenite shell starts to precipitate in the remaining melt. Further growth of eutectic graphite occurs by diffusion of carbon atoms from the melt through the austenite shell (divorced eutectic), which explains the relatively small size of the eutectic graphite nodules.[47,48]

On the other hand, in UST SG irons, a completely ferritic matrix is observed (see Figure 5b). During the eutectoid solid-state transformation, the high nodule count of the extremely fine graphite accelerated the rejection of carbon atoms from austenite; for that reason, the fully ferritic matrix is observed in all UST specimens. Table 3 summarizes the microstructure evolutions for both produced SG irons. The remarkable increase in the nodule count results in a decrease in the carbon diffusion path in austenite; hence, the rejection of the C-atoms from austenite during the eutectoid transformation will proceed much faster and fully ferritic matrix will result.

Nine locations below the sonotrode were selected for the nodule count measurements of the UST irons (see Figure 6). The graphite nodule diameter ranged between 6 and 9 µm with total nodules count ranging between 900 to more than 2000 nodules per mm^2 (see Figure 7). The highest nodule count ≈ 2100 nodules per mm^2 with extremely fine graphite nodules observed along the stream jet propagation area (60 mm deep away from the sonotrode) and then gradually decreases to ≈ 1500 nodules per mm^2 in the locations near the bottom and at the bottom edges. However, the lowest nodule count ≈ 1000 nodules per mm^2 was noticed in the locations near the edges of top. The large mechanical shock wave, associated with the cavitation collapse below the sonotrode, can induce an effective refinement of the microstructural constituents of the solidifying iron. Possible mechanisms of such refinement may be discussed in the following:

Wand et al.[49] suggested that during the solidification process under ultrasonic processing, the sonotrode could be considered as an additional chilling source for the melt and

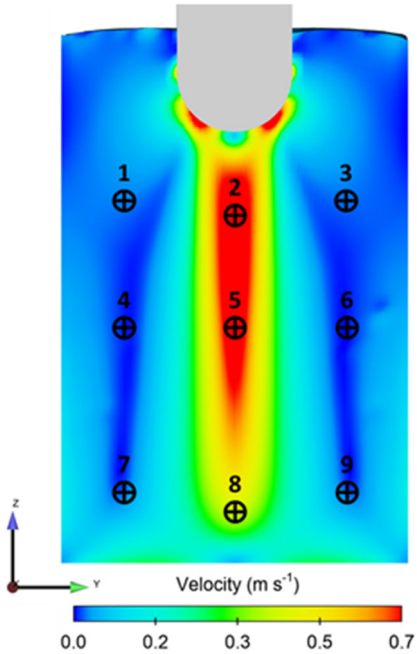

Figure 6. Sample locations in the UST mold that were selected for graphite morphology evaluation.

the tip surface of the sonotrode continuously sends solidified crystals into the melt. Therefore, the immersed water-cooled sonotrode in the molten iron will induce a rather high chilling influence on the adjacent volume of the melt, which in turn, enhances the formation of both primary graphite as well as primary austenite dendrites in the chilled volume of the melt.

With carbon equivalent (C.E) more than 4.5, primary graphite normally precipitates from the melt. However, with rather intensive chilling, the associated high degrees of eutectic undercooling will shift the eutectic C-content to higher values, leading to the precipitation of primary dendrites of austenite and the formation of an extremely fine graphite nodules observed in Figure 7 at the marked locations 2, 5 and 8.[48] Additionally, the chilled crystals, nucleated at the sonotrode surface, can be detached from the sonotrode during the UST streaming and the solid fragments may be showered into the melt and can be responsible for enhanced nucleation and further structural refinement.[49] Showering may be, to a lower extent, also related to the chilling effect of cold air above the open surface of the solidifying melt in the mold, with further

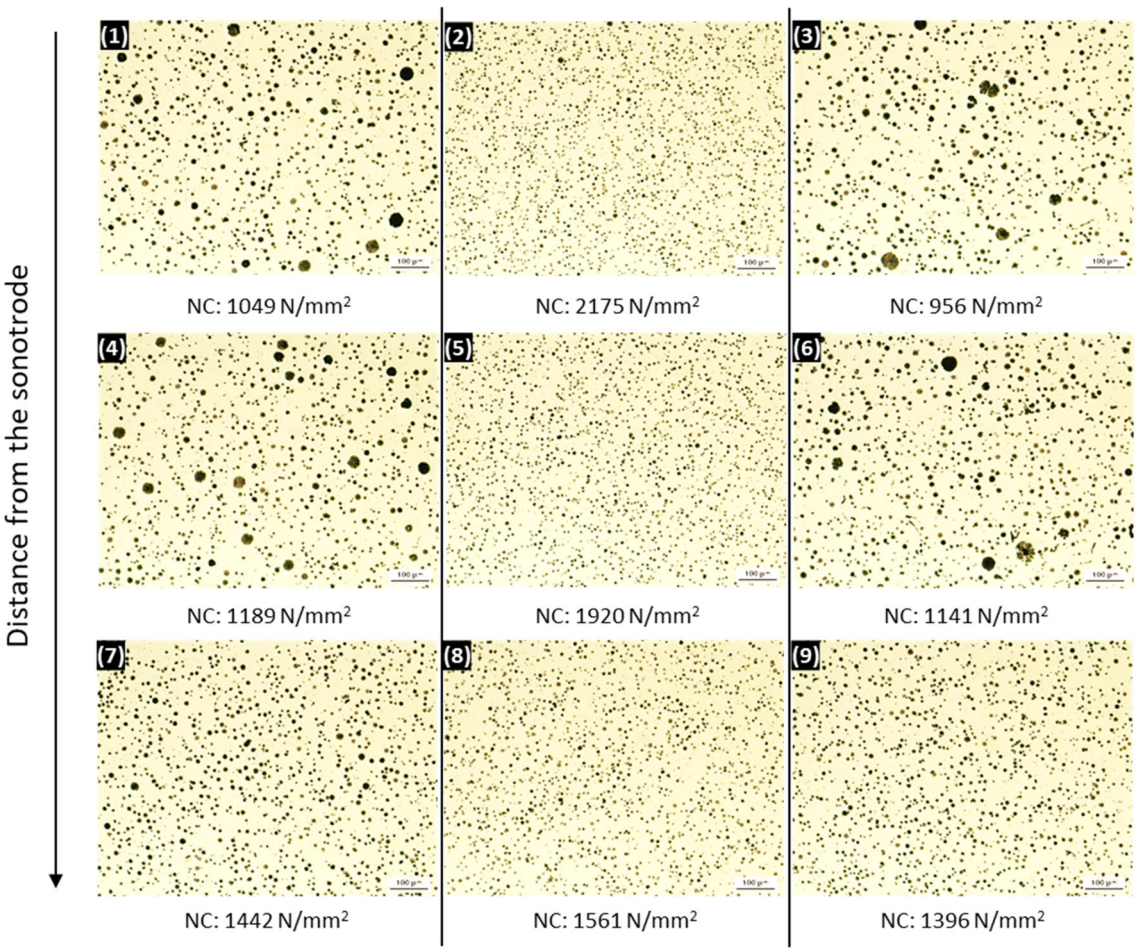

Figure 7. Nodule count and morphology of the graphite at different locations of the UST mold. The measured nodule counts are the average of five fields of view at each location.

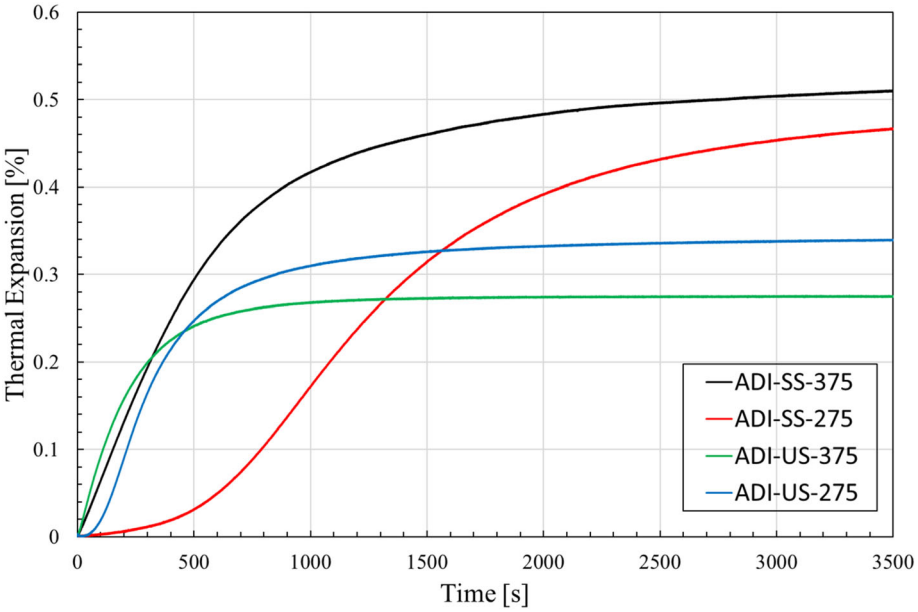

Figure 8. The dilatometry curve of the different investigated samples austempered at 275 °C and 375 °C, SS: conventional solidification sample, US: ultrasonic treated sample.

detachment of the chilled fragments due to the disturbance caused by UST.

It should be noticed that the extreme high nucleation level in the molten iron is due to fragmentation of both primary graphite as well as eutectic and primary austenite dendrites will decrease the undercooling during the eutectic solidification; as a consequent result, the eutectic solidification will proceed according to the stable reaction, where the liquid metal solidifies according to the reaction: Liquid (L) → Austenite (γ) + Graphite (G) with no chance for the metastable reaction to form: L → γ + Carbides. This might explain the complete absence of any carbide formation in the dynamically solidified specimens.

Later, Khosro Aghayani et al.[50] intimated that the very large shocks, resulting from the cavitation collapse, would move through those solid fragments, adjacent to the collapse zone and induce unusual levels of mechanical damage, leading to fragmentation or multiplication and formation of well-distributed fine structure. Furthermore, Ohno et al.[51] proposed that the UST streaming near the mold walls may lead to the detachment of the fine equiaxed chilled crystals formed at the mold wall, and throwing them into the undercooled melt in the vicinity of the mold wall, where they may act as additional centers of crystallization. This might clarify the higher nodule count and the finer graphite structure observed in the areas near the wall in the bottom of the mold (locations Nr. 7 and 9) than the area near the upper part of the mold (locations Nr. 1, 3, 4, and 6). As shown in Figure 3, with further progress of solidification, the effect of UST fades out as a result of the increased viscosity of the melt, arising from the increased solid volume fraction formed during solidification. As the velocity near the mold bottom approaches zero, the acoustic stream is circulated toward the mold's walls, then rising upward with low velocities. The primary graphite nodules formed near the mold walls, thus, have sufficient time for growth in the molten iron and the relatively coarse graphite nodules can be easily distinguished at locations 1, 3, 4 and 7 (see Figure 7).

Ausferrite Formation in ADI

Figure 8 illustrates the dilatometric charts of different UST SG iron. The relative expansion of the samples was determined according to the following equation:

$$\boldsymbol{\varepsilon} = \frac{\mathbf{L} - \mathbf{L}_o}{\mathbf{L}_o} \times 100[\%] \qquad \text{Eqn. 3}$$

where $\mathbf{L}_o$ and $\mathbf{L}$ are the initial and final lengths of the sample, respectively.

In the statically solidified samples, the rate of the ausferrite formation, expressed in terms of thermal expansion, is much faster in the samples austempered at higher temperatures of 375 °C. The rather longer incubation period of the samples austempered at 275 °C is related to the lower diffusion rate at such low temperatures. At the beginning of the ausferrite transformation, the thermal expansion and hence the transformations kinetics proceed at higher rate in the UST samples compared to statically solidified ones. This may be explained in view of two interlinked factors:

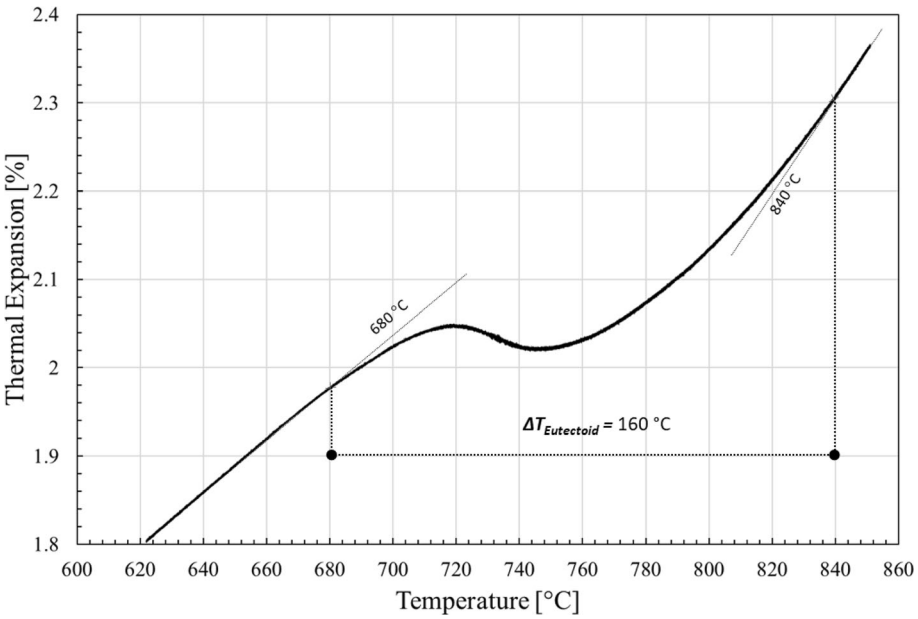

Figure 9. Part of the dilatation chart during continuous cooling of the ductile iron sample. The investigated sample were slowly heated to 900 °C at 0.1 K/s, held at that temperature for 15 min, and then slowly cooled at 0.1 K/s.

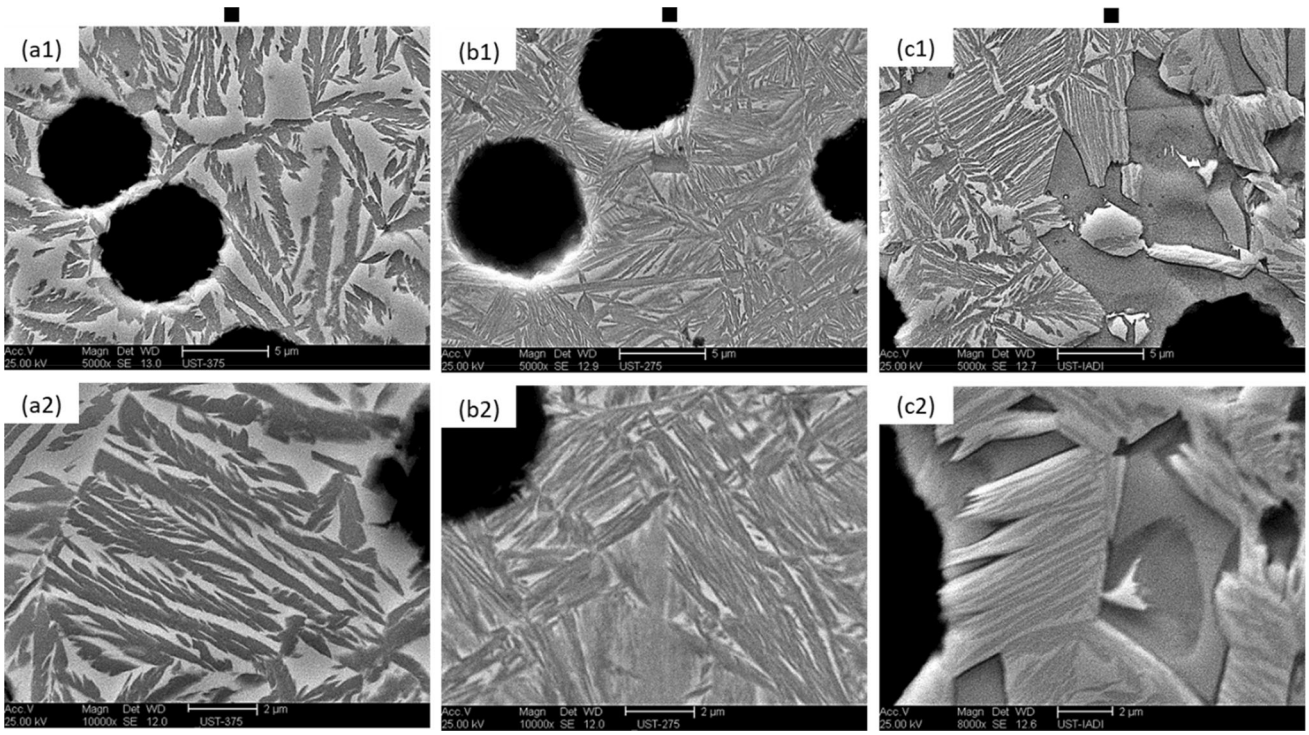

Figure 10. SEM micrographs of different ADI samples at two different magnifications, austempered at different austenitization ($T\gamma$) and austempering (TQ) temperatures; (a1-a2) $T\gamma$ = 900 °C, TQ = 275 °C, (b1-b2) $T\gamma$ = 900 °C, TQ = 375 °C, (c1-c2) $T\gamma$ = 820 °C, TQ = 325 °C.

i. The rather high nodule count in the UST samples shortens the interspace between fine graphite nodules, hence reducing the carbon diffusion path in austenite and enhances the transformation rate of ausferrite.[18]

ii. Moreover, the ultrafine graphite nodules enhance the number of eutectic cells formed during the eutectic reaction leading to an increased intercellular surface area, where the ferrite needles start to nucleate during the ausferrite transformation.[3]

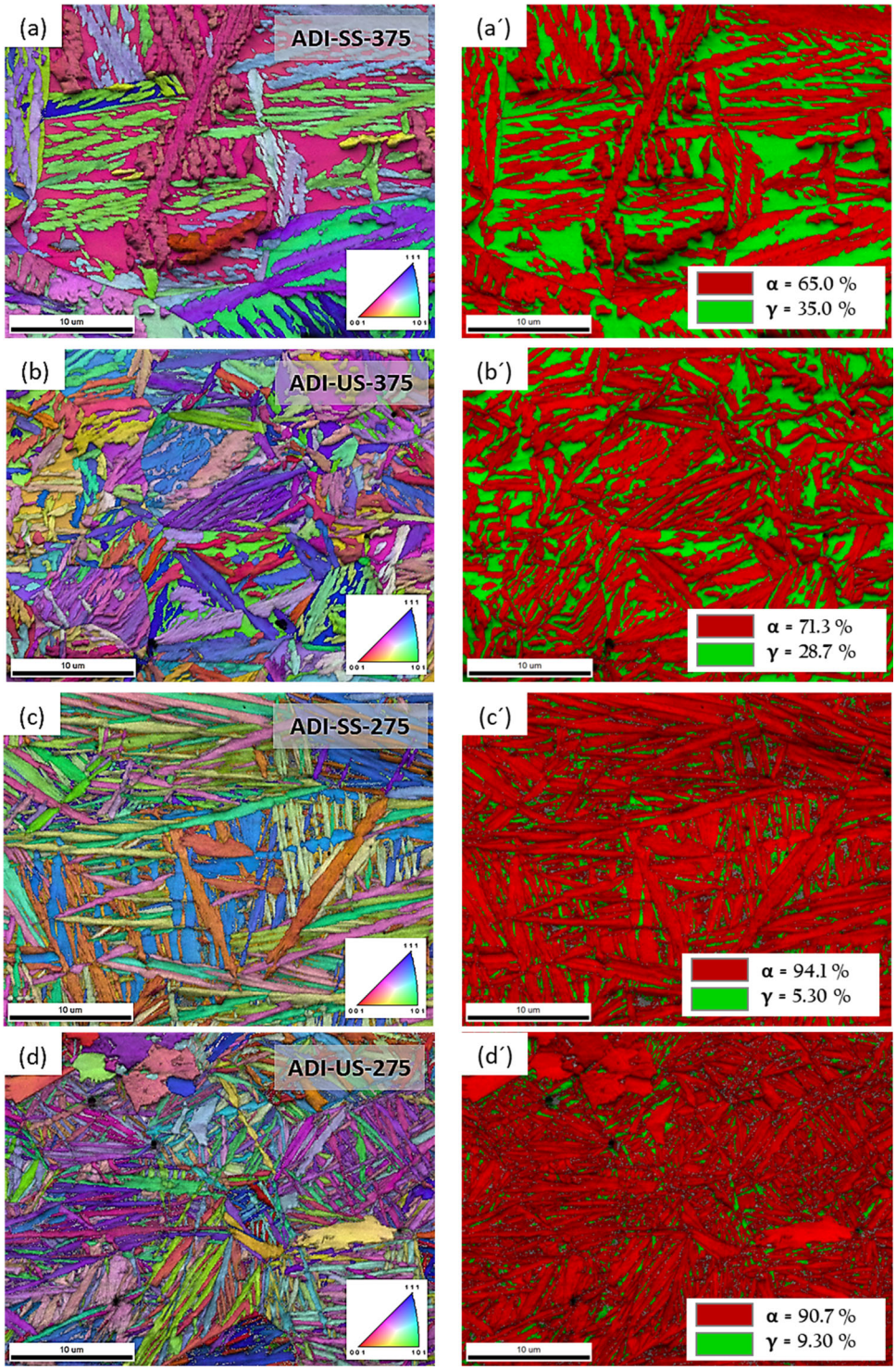

***Figure 11.** a The inverse pole figure orientation map (IPF) combined with image quality map (IQ) of the ausferrite in the ADI-SS-375 sample; (a´) phase distribution map in (a); (b) IPF orientation map combined with IQ map of the ausferrite in the ADI-US-375 sample; (b´) phase distribution map in (b); (c) IPF orientation map combined with IQ map of the ausferrite in the ADI-SS-275 sample; (c´) phase distribution map in (c); (d) IPF orientation map combined with IQ map of the ausferrite in the ADI-US-275 sample (d´) phase distribution map in (d).*

Table 4. Microhardness Values of the ADI Specimens Produced Under Static and Dynamic Solidification Conditions

Sample	ADI-SS-375	ADI-US-375	ADI-SS-275	ADI-US-275
Microhardness, HV*	290	341	370	430

*The indicated values are average of five measurements.

Both factors i and ii simultaneously contribute to the acceleration of the ausferrite transformation after ultrasonic treatment of the solidifying molten iron. Figure 8 shows that the ausferrite transformation curves reach plateau, which is the total time required for the cessation and completion of the ausferrite transformation in dramatically shorter times for the UST samples compared to the statically solidified ones. The transformation time resulted from the UST samples was four times shorter than the transformation time resulted in the statically solidified samples. An interesting phenomenon can be also observed from Figure 8. In UST samples, the total thermal expansion resulting from the ausferrite formation is only 50–60% of the thermal expansion of the statically solidified samples. This may be explained in the following: During the austenitization stage at 900 °C of the austempering heat treatment cycle, the carbon solubility in austenite increases and this occurs through the partial dissolution of graphite nodules into the austenite matrix. The remarkable increase of the graphite/austenite surface area in the UST samples can enhance the carbon dissolution process, and thin gaps may develop at the G / γ interface. Such gaps may exert a cushioning effect which can absorb, or damp certain fraction of the expansion associated with the ausferrite formation, hence the total apparent expansion measured by the dilatometer will be decreased as shown in Figure 8. This analysis may look speculative and need further confirming experiments.

To accurately select the intercritical austenitization temperature to produce an IADI grade, a typical dilatation curve was plotted to detect the eutectoid transformation of the austenite which is defined by the start and end temperatures (Ar1, Ar3). The ductile iron sample was slowly heated to 900 °C at a rate of 0.1 K/s and held at this temperature for 15 min. The sample then was slowly cooled to room temperature at a rate of 0.1 K/s. The eutectoid transformation temperatures of the austenite were determined by the deviation from linearity using the tangent method as shown in Figure 9.

Figure 10 illustrates the SEM micrographs of the UST ADI specimens with the main features described as follows: At low austempering temperature of 275 °C, very fine graphite spheroids are dispersed in a matrix of a nanostructured ausferrite (nano-size ferrite needles separated by retained austenite thin films also in nano-size). Much more refined ausferritic structure is observed in Figure 9a; as a consequence of enhanced ferrite nucleation at a higher degree of undercooling, lower austempering temperatures seem to increase the volume fraction of ferrite on the account of austenite. Small austenite blocks could be also observed in the matrix.

At high austempering temperature of 375 °C, increasing the austempering temperature to 375 °C leads to coarsening of the ausferrite from the parent austenite together with the increased C- diffusion rate which renders ferrite to be coarser with feathery morphology (Figure 9b). Furthermore, remarkable ausferritic bands with an extremely fine and short ferritic lathes were located beside the feathery ausferrite structure in the UST samples. These bands should greatly enhance and strengthen this grade of ADI. Moreover, a high amount of retained austenite blocks could be seen in the matrix.

Dual-Phase ADI is produced by applying partial austenitization heat treatment in the intercritical temperature range, where the austenite + ferrite + graphite phases coexist. The microstructure of the intercritically austenitized ductile iron consists of ausferrite and proeutectoid ferritic islands in the ausferrite continuous phase. Introducing free ferrite in the matrix would provide additional refinement for the ausferrite. As shown in Figure 9c, the interface between free ferrite and austenite offers additional nucleation sites for ausferrite nucleation.

The EBSD analysis of the ADI samples austempered at high and low austempering temperatures at the two different solidification conditions is shown in Figure 11. In the static solidification condition, the average thickness of ferrite lathe is 700 nm in the ADI samples austempered at 375 °C and 500 nm in the ADI samples austempered at 275 °C. Significantly refined ausferritic structure could be observed in the ultrasonically treated ADI samples. The average thickness of the ferrite lath is about 400 nm and 100 nm in the US-ADI samples austempered at 375 °C and 275 °C, respectively (see Figure 11a–d). Moreover, according to the phase distribution maps (see Figure 11a´–d´), it should be noticed that the volume fraction of the ferrite in all ultrasonically treated ADI samples is much higher than statically solidified ADI samples. This happens due to the high nodule count in the UST samples, which significantly enhances the transformation rate of the ausferrite.

Table 4 shows the measured microhardness values of the ADI samples austempered at temperatures of 275 °C and 375 °C in both static and dynamically solidified conditions. The measured values confirmed the positive impact of the refined ausferritic structure in the ultrasonically treated ADI samples on the mechanical properties. These results

are in agreement with the established fact that more refined structure often leads to an exceptional combination of mechanical properties such as high strength and high ductility properties.

Conclusions

In this investigation, ultrasonic treatment was successfully used to produce SG iron with ultrafine graphite structure in a ferritic matrix and ADI alloys with a fine ausferrite structure. The following remarks could be concluded:

CFD Simulation Analysis

A new CFD model was used to numerically simulate UST treatment in the molten iron. Ultrasonic waves penetrated the molten SG iron like a stream jet with a maximum speed of 0.7 m/s and gradually decreased to zero at the bottom of the mold. When the stream jet reached the bottom of the mold, it swept away at the edges forming a vortex flow and causing a circulation and mixing movement in the melt.

For the Ultrasonically Treated SG Irons

The metallographic analysis revealed an extremely ultrafine graphite structure. The graphite nodules diameter ranging between 6 and 9 μm with total nodule count ranging between 900 to more than 2000 nodules per mm^2. The highest nodule counts and extremely fine graphite nodules were observed along the stream jet propagation area (60 mm deep away from the sonotrode) and then gradually decrease in the locations near the bottom and in the bottom edges. The lowest nodule count was noticed in the locations near the edges of top surface as these locations had the lowest stream velocity. Furthermore, fully ferritic matrix was observed in all UST SG iron.

For the Ultrasonically Treated ADI Alloys

Different ADI alloys were produced using a quenching dilatometer. The dilatometry curves demonstrated that with increasing the nodule count of graphite in the matrix, the transformation time resulted from the UST samples was four times shorter than the transformation time resulted from statically solidified samples. SEM micrographs for the ADI alloys showed an extremely fine and short ausferrite structure together with small austenite blocks in the matrix. A dual-phase IADI alloy was also produced by applying partial austenitization heat treatment in the intercritical temperature range. In dual-phase IADI alloy, it was demonstrated that introducing free ferrite in the matrix would provide additional refinement for the ausferrite.

Acknowledgements

Authors would like to deeply thank Mr. O. Michael, Mr. M. Wilke and Mr. K. Harnisch from Otto-von-Guericke-Magdeburg University, Institute of Materials Engineering and Joining Technology (IWF) for their valuable contribution in performing the EBSD study reported in this research.

Author Contributions A. Nofal, A. Volochko, R. Bähr, and M. Ahmed contributed to conceptualization; A. Volochko and M. Kovalko contributed to methodology; E. Riedel and M. Ahmed contributed to software; E. Riedel and M. Ahmed contributed to validation; M. Ahmed, M. Kovalko, and E. Riedel contributed to formal analysis and investigation; M. Ahmed, E. Riedel, and M. Kovalko contributed to resources; M. Ahmed, E. Riedel, and M. Kovalko contributed to data curation; M. Ahmed contributed to writing—original draft preparation; A. Nofal, R. Bähr, and M. Ahmed contributed to writing—review and editing; M. Ahmed, A. Nofal, and E. Riedel contributed to visualization; and A. Nofal, R. Bähr and A. Volochko contributed to supervision. All authors have read and agreed to the published version of the manuscript.

Funding

Open Access funding enabled and organized by Projekt DEAL. This work was conducted in the frame of scientific collaboration between the Academy of Scientific Research and Technology (ASRT), Egypt and the National Academy of Sciences (NAS), Belarus under the project title, Development of Casting Alloys and Processes.

Availability of Data and Materials

The data used to support the findings of this study are available from the corresponding authors upon request.

Conflict of interest The authors declare that they have no conflicts of interest.

REFERENCES

1. C. Labrecque, Review ductile iron: fifty years of continuous development. Can. Metall. Q. **37**, 343–378 (1998). https://doi.org/10.1016/S0008-4433(98)00031-7

2. R.A. Harding, The production, properties and automotive applications of austempered ductile iron. Kovove Mater. **45**(1), 1–16 (2007)
3. A. Nofal, Advances in the metallurgy and applications of ADI. J. Metall. Eng. (ME) **2**, 1–18 (2013)
4. X. Guo, D.M. Stefanescu, L. Chuzhoy, M.A. Pershing, G.L. Biltgen, A mechanical properties model for ductile iron. AFS Trans. **105**, 47–54 (1997)
5. E. Fraś, H. López, Eutectic Cells and Nodule Count—An Index of Molten Iron Quality. Inter Metalcast **4**, 35–61 (2010). https://doi.org/10.1007/BF03355497
6. Z. Wang, X. Zhang, F. Xu, K. Qian, K. Chen, Effect of nodularity on mechanical properties and fracture of ferritic spheroidal graphite iron. China Foundry **16**, 386–392 (2019). https://doi.org/10.1007/s41230-019-9080-z
7. F. Zanardi, F. Bonollo, G. Angella, N. Bonora, G. Iannitti, A. Ruggiero, A Contribution to new material standards for ductile irons and austempered ductile irons. Inter Metalcast **11**, 136–147 (2017). https://doi.org/10.1007/s40962-016-0095-6
8. ASTM E2567-16a. *Test Method for Determining Nodularity And Nodule Count In Ductile Iron Using Image Analysis;* ASTM International: West Conshohocken, PA, 2016. Available online: www.astm.org.
9. T. Kanno, Y. Iwami, I. Kang, Prediction of graphite nodule count and shrinkage tendency in ductile cast iron, with 1 cup thermal analysis. Inter Metalcast **11**, 94–100 (2017). https://doi.org/10.1007/s40962-016-0111-x
10. M. Nadeem Bhat, D.M. Afzal Khan, K.K. Singh, Effect of preconditioning and inoculation on graphite nodule count and their size distribution in spheroidal graphite (SG) cast iron: a study to minimise rejection of castings due to shrinkage porosity. Inter Metalcast **13**, 89–97 (2019). https://doi.org/10.1007/s40962-018-0230-7
11. S.N. Lekakh, Communication: characterization of spatial distribution of graphite nodules in cast iron. Inter Metalcast **11**, 743–748 (2017). https://doi.org/10.1007/s40962-016-0128-1
12. S.N. Lekakh, X. Zhang, W. Tucker, H.K. Lee, T. Selly, J.D. Schiffbauer, Micro-CT quantitative evaluation of graphite nodules in SGI. Inter Metalcast **14**, 318–327 (2020). https://doi.org/10.1007/s40962-019-00354-9
13. K.M. Pedersen, N.S. Tiedje, Graphite nodule count and size distribution in thin-walled ductile cast iron. Mater. Charact. **59**, 1111–1121 (2008). https://doi.org/10.1016/j.matchar.2007.09.001
14. A.D. Sosa, M.D. Echeverría, O.J. Moncada, N. Míngolo, J.A. Sikora, Influence of nodule count on residual stresses and distortion in thin wall ductile iron plates of different matrices. J. Mater. Process. Technol. **209**, 5545–5551 (2009). https://doi.org/10.1016/j.jmatprotec.2009.05.010
15. Y. Tanaka, Z. Yang, K. Miyamoto, Evaluation of fatigue limit of spheroidal graphite cast iron. Mater. Trans. JIM. **36**, 749–756 (1995). https://doi.org/10.2320/matertrans1989.36.749
16. K.A. Kasvayee, *PhD thesis, Microstructure and deformation behaviour of ductile iron under tensile loading;* Jönköping University, School of Engineering: Jönköping, 2015, ISBN 9187289105.
17. Y. Amran, A. Katsman, P. Schaaf, M. Bamberger, Influence of copper addition and temperature on the kinetics of Austempering in ductile iron. Metall and Materi Trans B **41**, 1052–1058 (2010). https://doi.org/10.1007/s11663-010-9388-y
18. E. Fraś, M. Górny, E. Tyrała, H. Lopez, Effect of nodule count on austenitising and austempering kinetics of ductile iron castings and mechanical properties of thin walled iron castings. Mater. Sci. Technol. **28**, 1391–1396 (2012). https://doi.org/10.1179/1743284712Y.0000000088
19. E. Colin-García, A. Cruz-Ramírez, J.A. Romero-Serrano, R.G. Sánchez-Alvarado, V.H. Gutiérrez-Pérez, G. Reyes-Castellanos, Nodule count effect on microstructure and mechanical properties of hypo-eutectic ADI alloyed with nickel. J min metall B Metall **57**, 115–124 (2021). https://doi.org/10.2298/JMMB200403009C
20. M.M. Mourad, K.M. Ibrahim, M.M. Ibrahim, A.A. Nofal, Optimizing the properties of thin wall austempered ductile iron. *Proceedings of 68th World Foundry Congress*, 161–166. (2008)
21. G.S.B. Lebon, I. Tzanakis, K. Pericleous, D. Eskin, P.S. Grant, Ultrasonic liquid metal processing: The essential role of cavitation bubbles in controlling acoustic streaming. Ultrason. Sonochem. **55**, 243–255 (2019). https://doi.org/10.1016/j.ultsonch.2019.01.021
22. D.G. Eskin, I. Tzanakis, F. Wang, G.S.B. Lebon, T. Subroto, K. Pericleous, J. Mi, Fundamental studies of ultrasonic melt processing. Ultrason. Sonochem. **52**, 455–467 (2019). https://doi.org/10.1016/j.ultsonch.2018.12.028
23. D.G. Eskin, Ultrasonic processing of molten and solidifying aluminium alloys: overview and outlook. Mater. Sci. Technol. **33**, 636–645 (2017). https://doi.org/10.1080/02670836.2016.1162415
24. S. Wang, Z.P. Guo, X.P. Zhang, A. Zhang, J.W. Kang, On the mechanism of dendritic fragmentation by ultrasound induced cavitation. Ultrason. Sonochem. **51**, 160–165 (2019). https://doi.org/10.1016/j.ultsonch.2018.10.031
25. N. Srivastava, G.P. Chaudhari, Grain refinement in ultrasonicated binary aluminium alloys. J. Cryst. Growth **532**, 125415 (2020). https://doi.org/10.1016/j.jcrysgro.2019.125415
26. G. Chen, M. Yang, Y. Jin, H. Zhang, F. Han, Q. Chen, Z. Zhao, Ultrasonic assisted squeeze casting of a wrought aluminum alloy. J. Mater. Process. Technol.

266, 19–25 (2019). https://doi.org/10.1016/j.jmatprotec.2018.10.032
27. O. Yoshiaki, A. Goro, T. Susumu, S. Akira, H. Hideki, N. Keiji, Effects of Ultrasonic vibration on solidification structures of cast iron. J Japan Foundrmen's Soc. **67**, 325–330 (1995). https://doi.org/10.11279/imono.67.5_325
28. X. Zhang, J. Kang, S. Wang, J. Ma, T. Huang, The effect of ultrasonic processing on solidification microstructure and heat transfer in stainless steel melt. Ultrason. Sonochem. **27**, 307–315 (2015). https://doi.org/10.1016/j.ultsonch.2015.05.041
29. I. Yoshida, H. Ohsone, Effect of ultrasonic vibration on the metallurgical properties of steel. J. Phys. Colloques. **42**, 1153–1158 (1981). https://doi.org/10.1051/jphyscol:19815178
30. J. Kang, X. Zhang, S. Wang, J. Ma, T. Huang, The comparison of ultrasonic effects in different metal melts. Ultrasonics **57**, 11–17 (2015). https://doi.org/10.1016/j.ultras.2014.10.004
31. R. Voigt, P. Lynch, T. Grenko, Cast iron solidification with non-contact acoustic stimulation. Inter Metalcast **3**, 79–86 (2009). https://doi.org/10.1007/BF03355461
32. G.I. Eskin, D.G. Eskin, Effects of ultrasonic (Cavitation) melt processing on the structure refinement and property improvement of cast and worked aluminum alloys. MSF **396–402**, 77–82 (2002)
33. B.E. Noltingk, E.A. Neppiras, Cavitation produced by Ultrasonics. Proc. Phys. Soc. B **63**, 674–685 (1950). https://doi.org/10.1088/0370-1301/63/9/305
34. S. Panneerselvam, S.K. Putatunda, Processing of nanostructured austempered ductile cast iron (ADI) by a novel method. Int J Metall Met Phys **3**, 1–11 (2018). https://doi.org/10.35840/2631-5076/9220
35. M. Soliman, A. Nofal, H. Palkowski, Alloy and process design of thermo-mechanically processed multiphase ductile iron. Mater. Des. **87**, 450–465 (2015). https://doi.org/10.1016/j.matdes.2015.07.159
36. D. Myszka, K. Wasiluk, E. Skoek, W. Świątnicki, Nanoausferritic matrix of ductile iron. Mater. Sci. Technol. **31**, 829–834 (2015). https://doi.org/10.1179/1743284714Y.0000000733
37. E. Riedel, M. Liepe, S. Scharf, Simulation of ultrasonic induced cavitation and acoustic streaming in liquid and solidifying aluminum. Metals **10**, 476 (2020). https://doi.org/10.3390/met10040476
38. E. Riedel, I. Horn, N. Stein, H. Stein, R. Bähr, S. Scharf, Ultrasonic treatment: a clean technology that supports sustainability in casting processes. Procedia CIRP **80**, 101–107 (2019). https://doi.org/10.1016/j.procir.2019.01.110
39. W.L. Guesser, C.L. Lopes, P.A.N. Bernardini, Austempered ductile iron with dual microstructures: effect of initial microstructure on the austenitizing process. Inter Metalcast **14**, 717–727 (2020). https://doi.org/10.1007/s40962-019-00397-y
40. M. Soliman, A. Nofal, H. Palkowski, Effect of thermo-mechanical processing on structure and properties of dual-phase matrix ADI with different Si-Contents. Inter Metalcast **14**, 853–860 (2020). https://doi.org/10.1007/s40962-020-00477-4
41. R.B. Gundlach, Heat treatments to develop high-strength ferritic ductile iron. Inter Metalcast **14**, 1065–1077 (2020). https://doi.org/10.1007/s40962-020-00489-0
42. S. Grenier, C. Labrecque, A. Bhattacharjee, R. Gundlach, B. Kroka, M. Riabov, Inter-laboratory study of nodularity and nodule count of ductile iron by image analysis. Inter Metalcast **8**, 51–63 (2014). https://doi.org/10.1007/BF03355582
43. Santa Fe, NM: Flow Science, Inc. *FLOW-3D®;* USA, 2019.
44. Santa Fe, NM: Flow Science, Inc. *FLOWSight®;* USA, 2019.
45. J. Campbell, Effects of vibration during solidification. Int. Metals Rev. **26**, 71–108 (1981). https://doi.org/10.1179/imtr.1981.26.1.71
46. J. Kang, X. Zhang, Y. Hu, J. Ma, Y. Hu, T. Huang, Ultrasonic treatment of the 304 stainless steel melt. ISIJ Int. **54**, 281–287 (2014). https://doi.org/10.2355/isijinternational.54.281
47. J. Lacaze, M. Castro, G. Lesoult, Solidification of spheroidal graphite cast irons—II. numerical simulation. Acta Mater. **46**, 997–1010 (1998). https://doi.org/10.1016/S1359-6454(97)00282-6
48. A. Regordosa, U. de LaTorre, A. Loizaga, J. Sertucha, J. Lacaze, Microstructure changes during solidification of cast irons: effect of chemical composition and inoculation on competitive spheroidal and compacted graphite growth. Inter Metalcast **14**, 681–688 (2020). https://doi.org/10.1007/s40962-019-00389-y
49. G. Wang, P. Croaker, M. Dargusch, D. McGuckin, D. StJohn, Simulation of convective flow and thermal conditions during ultrasonic treatment of an Al-2Cu alloy. Comput. Mater. Sci. **134**, 116–125 (2017). https://doi.org/10.1016/j.commatsci.2017.03.041
50. M. Khosro Aghayani, B. Niroumand, Effects of ultrasonic treatment on microstructure and tensile strength of AZ91 magnesium alloy. J. Alloy. Compd. **509**, 114–122 (2011). https://doi.org/10.1016/j.jallcom.2010.08.139
51. Ohno, A. *Solidification*: *The Separation Theory and its Practical Applications;* Springer International Publishing: Cham, 20, ISBN 9783642955372